

Forecasting the population properties of merging black holes

Viola De Renzi ^{1,2,*}, Francesco Iacovelli ³, Davide Gerosa ^{1,2}, Michele Mancarella ⁴ and Costantino Pacilio ^{1,2}

¹*Dipartimento di Fisica “G. Occhialini”, Università degli Studi di Milano-Bicocca, Piazza della Scienza 3, 20126 Milano, Italy*

²*INFN, Sezione di Milano-Bicocca, Piazza della Scienza 3, 20126 Milano, Italy*

³*Département de Physique Théorique and Gravitational Wave Science Center, Université de Genève, 24 quai Ernest Ansermet, 1211 Genève 4, Switzerland*

⁴*Aix-Marseille Université, Université de Toulon, CNRS, CPT, Marseille, France*

(Dated: March 14, 2025)

Third-generation gravitational-wave detectors will observe up to millions of merging binary black holes. With such a vast dataset, stacking events into population analyses will arguably be more important than analyzing single sources. We present the first application of population-level Fisher-matrix forecasts tailored to third-generation gravitational-wave interferometers ^a. We implement the formalism first derived by Gair *et al.* [MNRAS 519, 2736 (2023)] and explore how future experiments such as Einstein Telescope and Cosmic Explorer will constrain the distributions of black-hole masses, spins, and redshift. Third-generation detectors will be transformative, improving constraints on the population hyperparameters by several orders of magnitude compared to current data. At the same time, we highlight that a single third-generation observatory and a network of detectors will deliver qualitatively similar performances. Obtaining precise measurements of some population features (e.g. peaks in the mass spectrum) will require only a few months of observations while others (e.g. the fraction of binaries with aligned spins) will instead require years if not decades. We argue population forecasts of this kind should be featured in white papers and feasibility studies aimed at developing the science case of future gravitational-wave interferometers.

I. INTRODUCTION

Gravitational-wave (GW) astronomy is quickly turning into a big-data discipline. We now have hundreds of detections, which will become thousands in a few years and millions in a few decades [1, 2]. The focus of GW inference is thus shifting from inferring the parameters of single events to those of the entire population of detected sources.

Current population analyses of LIGO/Virgo data [3–5] are providing precious information on the physical processes that drive black holes (BHs) and neutron stars to merger [6–8]. In particular, there is strong indication that the merger rate of stellar-mass BHs decreases steeply for sources of masses $\gtrsim 60 M_{\odot}$ but piles up at $\sim 35 M_{\odot}$. The spins of merging stellar-mass BHs show some preference for dimensionless magnitudes $\lesssim 0.3$ and some degree of co-alignment with the orbital angular momentum of the respective binaries. Besides marginal distributions, the growing GW dataset is now allowing us to explore correlations between parameters [9–16].

State-of-the-art population analyses are tackled using hierarchical Bayesian statistics [17, 18]. In short, one assumes an underlying inhomogeneous Poisson process and marginalizes over the parameters of the single events (e.g. masses, spins, etc.) while retaining information on the “hyperparameters” that describe the entire population of sources (e.g. mass cutoffs, spectral indexes, etc.). Current state-of-the-art implementations rely on recycling

single-event posterior distributions for the computation of marginal integrals, as well as on injection campaigns to estimate selection biases via reweighted Monte Carlo integration [19, 20]. This requires careful handling of both finite-sampling and selection effects [21]. While under control for the time being, the feasibility of these techniques with much larger catalogs remains an open question.

The future of ground-based GW astronomy is under active planning, with flagship projects such as Einstein Telescope (ET) [22] and Cosmic Explorer (CE) [23] that promise to observe virtually all the BH binaries merging in the visible Universe, with detection rates of $\mathcal{O}(10^5/\text{yr})$ [2, 24]. At present, running full Bayesian schemes on such large catalogs is both too costly and premature, if feasible at all. Science forecasts largely rely on the Fisher information matrix formalism [25], which approximates the single-event likelihood in the high signal-to-noise ratio (SNR) limit. Fisher codes tailored to third-generation (3G) detectors include GWFAST [26], GWBENCH [27], GWFISH [28], TiDoFM [29], and the code used in Ref. [30]. All such codes provide forecasts for the parameter estimation of single events rather than of population parameters.

On the other hand, in the third-generation (3G) era the focus of GW science will definitely be on populations. With the exception of prominent outliers, it is easy to imagine how the analysis of a single event will not be relevant when there are millions of similar sources sitting next to it. Despite this quite obvious statement, current forecasts presented in “colored books” to funding agencies for the identification of the ET and CE science cases still rely on single-event analyses [2, 31–33]. We believe this is a severe limitation.

In this paper, we present the first population-level

* v.derenzis@campus.unimib.it

^a <https://github.com/CosmoStatGW/gwfast/tree/master/gwfast/population>

Fisher matrix implementation tailored to 3G detectors. The relevant equations have been developed by Gair *et al.* [34], who first wrote down the Fisher-like expansion of the population likelihood including selection effects. Their expressions have so far only been applied to toy models. Here we significantly broaden the scope of the analysis to state-of-the-art parameterized population models, presenting detailed predictions for 3G detectors. We argue forecasts of this kind should be featured in future design documents to appropriately assess the outstanding science we will be able to deliver with facilities of the caliber of ET and CE.

Section II introduces the Fisher formalism for both individual-event and population inference. Section III provides details on the implementation of our code, alongside a description of the population models used throughout this study. Section IV presents our population-inference results, with a particular focus on the detector network as well as the astrophysical distributions of masses, spins, and redshift. Finally, Sec. V summarizes our main findings and discusses their implications.

II. FORMALISM

In the following, d indicates the data of a single GW signal, $\{d\}$ indicates data of a set of signals, θ indicates the parameters of individual events, and λ indicates the hyperparameters describing the populations.

A. Single-event inference

Under the assumption that the noise is stationary and Gaussian, the likelihood of the event parameters is given by [35]

$$p(d|\theta) \propto \exp \left[-\frac{1}{2} (d - h(\theta) | d - h(\theta)) \right], \quad (1)$$

where $h(\theta)$ is the gravitational signal and $(\cdot | \cdot)$ indicates the noise-weighted inner product. For a given BH binary with true parameters $\bar{\theta}$, the elements of the Fisher information matrix are given by

$$\Gamma_{\theta,ij} \equiv - \left\langle \frac{\partial^2 \ln p(d|\theta)}{\partial \theta_i \partial \theta_j} \right\rangle \Big|_{\theta=\bar{\theta}} = \left(\frac{\partial h}{\partial \theta_i} \Big| \frac{\partial h}{\partial \theta_j} \right) \Big|_{\theta=\bar{\theta}}, \quad (2)$$

where the expectation value $\langle \cdot \rangle$ is taken over noise realizations. The covariance matrix is given by Γ_{θ}^{-1} such that the errors on each parameter θ_i are given by the diagonal elements $(\Gamma_{\theta}^{-1})_{ii}^{1/2}$. The Fisher matrix provides a Gaussian approximation to the likelihood that becomes increasingly accurate in the high-SNR limit. This is equivalent to approximating the posterior distribution $p(\theta|d)$ if one assumes that the prior over θ is flat across the support of the likelihood itself.

B. Population inference

The chosen population model is encoded in the probability distribution $p_{\text{pop}}(\theta|\lambda)$ that predicts the likelihood of compact objects merging with parameters θ for a given choice of the population λ . The population likelihood marginalized over the event rate is given by [17, 18]

$$p(\{d\}|\lambda) \propto p_{\text{det}}(\lambda)^{-N_{\text{det}}} \prod_{k=1}^{N_{\text{det}}} \int p(d_k|\theta) p_{\text{pop}}(\theta|\lambda) d\theta, \quad (3)$$

where N_{det} is the number of detected events in the catalog. While state-of-the-art, this expression assumes that GW events are statistically independent. This is an excellent approximation for LIGO/Virgo but a poorer one for ET and CE where multiple signals might overlap in the same stretch of data [36, 37]. Performing GW population analyses with overlapping signals is an unsolved problem.

The term $p_{\text{det}}(\lambda)$ in Eq. (3) is the fraction of detected events in the population described by λ , i.e.

$$p_{\text{det}}(\lambda) = \int p_{\text{det}}(\theta) p_{\text{pop}}(\theta|\lambda) d\theta \leq 1, \quad (4)$$

where $p_{\text{det}}(\theta)$ is the probability of observing a merging binary with parameters θ . For simplicity and as common practice in the field, we use the SNR as a detection statistics and set

$$p_{\text{det}}(\theta) = \frac{1}{2} \left\{ 1 + \text{erf} \left[\frac{\rho(\theta) - \rho_{\text{th}}}{\sqrt{2}} \right] \right\}, \quad (5)$$

where ρ_{th} is a fixed threshold and $\rho(\theta) = \sqrt{(h(\theta)|h(\theta))}$ is the optimal SNR. Equation (5) includes the variance of the SNR due to noise realizations but not the effect of multiple detectors [38]. We neglect this subtlety in favor of an efficient numerical implementation and use Eq. (5) also for detector networks, adding the SNRs of each instrument in quadrature. In particular, we set $\rho_{\text{th}} = 12$.

The Fisher-matrix approximation of the likelihood in Eq. (3) has been worked out in Ref. [34]. Assuming a true population described by $\bar{\lambda}$, the elements of the hyper-Fisher matrix are

$$\Gamma_{\lambda,ij} \equiv - \left\langle \frac{\partial^2 \ln p(\{d\}|\lambda)}{\partial \lambda^i \partial \lambda^j} \right\rangle \Big|_{\lambda=\bar{\lambda}}, \quad (6)$$

which we write as a sum of five leading contributions¹

$$\Gamma_{\lambda,ij} = \frac{N_{\text{det}}}{p_{\text{det}}(\lambda)} (\Gamma_{\text{I},ij} + \Gamma_{\text{II},ij} + \Gamma_{\text{III},ij} + \Gamma_{\text{IV},ij} + \Gamma_{\text{V},ij}), \quad (7)$$

¹ The symbol Γ_{λ} here indicates the hyper-Fisher matrix and not its single-event contribution as in Ref. [34]. With this notation, the components of Γ_{λ}^{-1} directly provide the hyperparameters errors and correlations for a detection catalog of N_{det} events. Compared to notation of Ref. [34], this is equivalent to adding a factor of N_{det} to the definition of Γ_{λ} . We have also factored out a common term $p_{\text{det}}^{-1}(\lambda)$ from $\Gamma_{\text{I-V}}$.

where

$$\Gamma_{\text{I},ij} = - \int \frac{\partial^2 \ln [p_{\text{pop}}(\bar{\theta}|\lambda) p_{\text{det}}^{-1}(\lambda)]}{\partial \lambda_i \partial \lambda_j} \Bigg|_{\lambda=\bar{\lambda}} p_{\text{det}}(\bar{\theta}) p_{\text{pop}}(\bar{\theta}|\bar{\lambda}) d\bar{\theta}, \quad (8)$$

$$\Gamma_{\text{II},ij} = \frac{1}{2} \int \frac{\partial^2 \ln \det(\Gamma_\theta + H)}{\partial \lambda_i \partial \lambda_j} \Bigg|_{\lambda=\bar{\lambda}} p_{\text{det}}(\bar{\theta}) p_{\text{pop}}(\bar{\theta}|\bar{\lambda}) d\bar{\theta}, \quad (9)$$

$$\Gamma_{\text{III},ij} = - \frac{1}{2} \int \frac{\partial^2 [(\Gamma_\theta + H)^{-1}]_{kl}}{\partial \lambda_i \partial \lambda_j} \Bigg|_{\lambda=\bar{\lambda}} \Gamma_{\theta,kl} p_{\text{pop}}(\bar{\theta}|\bar{\lambda}) d\bar{\theta}, \quad (10)$$

$$\Gamma_{\text{IV},ij} = - \int \frac{\partial^2 [P_k(\Gamma_\theta + H)^{-1}]_{kl}}{\partial \lambda_i \partial \lambda_j} \Bigg|_{\lambda=\bar{\lambda}} D_l p_{\text{pop}}(\bar{\theta}|\bar{\lambda}) d\bar{\theta}, \quad (11)$$

$$\Gamma_{\text{V},ij} = - \frac{1}{2} \int \frac{\partial^2 [P_k(\Gamma_\theta + H)^{-1} P_l]}{\partial \lambda_i \partial \lambda_j} \Bigg|_{\lambda=\bar{\lambda}} p_{\text{det}}(\bar{\theta}) p_{\text{pop}}(\bar{\theta}|\bar{\lambda}) d\bar{\theta}. \quad (12)$$

Here, Γ_θ is the single-event Fisher matrix defined in Eq. (2) and

$$P_i = \frac{\partial \ln p_{\text{pop}}(\theta|\lambda)}{\partial \theta_i} \Bigg|_{\theta=\bar{\theta}}, \quad (13)$$

$$H_{ij} = - \frac{\partial^2 \ln p_{\text{pop}}(\theta|\lambda)}{\partial \theta_i \partial \theta_j} \Bigg|_{\theta=\bar{\theta}}, \quad (14)$$

$$D_i = \frac{\partial p_{\text{det}}(\theta)}{\partial \theta_i} \Bigg|_{\theta=\bar{\theta}} = \frac{\partial p_{\text{det}}}{\partial \rho} \frac{\partial \rho}{\partial \theta_i} \Bigg|_{\theta=\bar{\theta}}. \quad (15)$$

From these expressions, one can compute the covariance matrix Γ_λ^{-1} and thus the errors on the population hyperparameters $(\Gamma_\lambda^{-1})_{ii}^{1/2}$.

In the limit where the uncertainties on the parameters of the individual sources are negligible, one has $\Gamma_\theta \rightarrow \infty$ which implies $\Gamma_{\text{II-V}} \rightarrow 0$ because $\Gamma_\theta + H \sim \Gamma_\theta$, hence $(\Gamma_\theta + H)^{-1} \rightarrow 0$, and $\partial \Gamma_\theta / \partial \lambda = 0$. The population Fisher matrix Γ_λ can thus be approximated with the first term Γ_{I} of Eq. (8), which we expect to be the dominant contribution in our forecasting exercise (cf. Ref. [34]). Note that Eqs. (8)-(12) are derived by averaging the population likelihood over noise realizations. This procedure ensures that the average impact of the noise bias is naturally included in the final Fisher expression, particularly in the term $\Gamma_{\text{IV},ij}$ through its dependence on Eq. (15). For further details, we refer the reader to Ref [34].

C. Interpretation

Equations (7–12) were computed assuming a Fisher-matrix description for the single-event likelihoods as well as large number of events, namely $N_{\text{det}} \rightarrow \infty$ [34]. The appropriate limit for a population Fisher analysis is that of many and well-measured GW signals. In this limit, the population Fisher matrix scales with the size of the catalog as $\Gamma_\lambda \propto N_{\text{det}}$, cf. Eqs. (4) and (7) for any given population with efficiency $p_{\text{det}}(\lambda)$.

Crucially, the expressions above provide the population Fisher matrix only up to additional corrections scaling with inverse powers of N_{det} . This implies that Γ_λ is not guaranteed to be positive definite, thus casting some issues on the interpretation of its inverse as a covariance matrix. In practice, however, all diagonal terms $(\Gamma_\lambda^{-1})_{ii}$ are positive and those cases where the Fisher matrix Γ_λ is non-positive definite are due to a small but negative eigenvalue. If off-diagonal terms are needed (e.g. when drawing corner plots), we regularize Γ_λ^{-1} by replacing the negative eigenvalue with its absolute value and projecting it back to the original coordinate space.

III. IMPLEMENTATION

A. Approximants and detectors

We implement the population Fisher-matrix formalism described above in the PYTHON programming language, leveraging the infrastructure of the single-event Fisher code GWFAST [26]. All derivatives with respect to λ are performed with automatic differentiation via JAX [39].

We use the IMRPHENOMXPHM [40–42] waveform model, and perform the single-event Fisher analysis in terms of the parameters $\tilde{\theta} = \{\mathcal{M}_z, \eta, \chi_1, \chi_2, \phi_{JL}, \phi_{12}, \theta_1, \theta_2, d_L, \alpha, \delta, \theta_{JN}, \psi, t_c, \phi_c\}$. These are the detector-frame chirp mass \mathcal{M}_z , the symmetric mass ratio η , the dimensionless spin magnitudes $\chi_{1,2}$, tilt angles $\theta_{1,2}$, the azimuthal spin angle $\phi_{1,2}$, the azimuthal angle ϕ_{JL} between the total and orbital angular momenta, the luminosity distance d_L , the sky position coordinates α, δ , the polar angle θ_{JN} between total angular momentum and the line of sight, the polarization angle ψ , the time of coalescence t_c and the phase at coalescence ϕ_c (see Ref. [24]). We assume a flat Λ CDM model with PLANCK18 parameters [43].

We add a regularization matrix to the Fisher $\Gamma_{\tilde{\theta}}$ [25], specifically targeting the sector associated with the spin magnitudes and angular spin parameters; this serves two purposes: avoiding singular matrices $\Gamma_{\tilde{\theta}}$ and incorporating information on the physical range of some parameters. Our regularization matrix is diagonal, with elements chosen as the inverse variances of the Gaussian distributions we impose. Specifically, the diagonal elements corresponding to the spin magnitudes, spin orientations, and azimuthal angles are $\{\sigma_{\chi_1}^{-2}, \sigma_{\chi_2}^{-2}, \sigma_{\phi_{JL}}^{-2}, \sigma_{\phi_{12}}^{-2}, \sigma_{\theta_1}^{-2}, \sigma_{\theta_2}^{-2}\} = \{1, 1, (2\pi)^{-2}, (2\pi)^{-2}, \pi^{-2}, \pi^{-2}\}$. All other elements are set to zero.

Note the set of parameters $\tilde{\theta}$ is not equivalent to the set θ entering our population analysis (see below), the difference being in the mass and redshift parameters. We rotate the Fisher matrix $\Gamma_{\tilde{\theta}}$ computed by GWFAST to obtain Γ_θ . In particular, one has $\Gamma_\theta = J^T \Gamma_{\tilde{\theta}} J$ where $J = d\tilde{\theta}/d\theta$ is the Jacobian of the rotation between the $\tilde{\theta}$ and the θ parameters. In practice, this means we are assuming the likelihood is Gaussian also in the θ parameters; this is

motivated by the large SNRs delivered by 3G detections.

We compare results obtained assuming a single, triangular shaped ET interferometer against a detector network composed of ET and two CE detectors [2, 33]. Specifically, we use the 10 km noise curve for ET from Ref. [2] assuming a nominal location in Sardinia, Italy, and CE noise curves² assuming two interferometers with arm lengths of 40 km and 20 km in the USA [27, 33, 44]. We set a minimum frequency of 2 Hz for ET and 5 Hz for CE. The effect of the Earth rotation on the signal is taken into account when computing single-event Fisher matrices with GWFAST.

B. Population models

The results presented in this work rely on a standard parametric population model $p_{\text{pop}}(\theta|\lambda)$ borrowed from current LIGO/Virgo/KAGRA analyses [5]. We tackle population inference on source-frame masses, spin magnitudes, spin tilts, and redshifts, i.e. $\theta = \{m_1, m_2, \chi_1, \chi_2, \theta_1, \theta_2, z, \Omega\}$. We assume that $p_{\text{pop}}(\theta|\lambda)$ is separable over the source parameters as follows

$$p_{\text{pop}}(\theta|\lambda) = p(m_1, m_2|\lambda_m)p(\chi_1|\lambda_\chi)p(\chi_2|\lambda_\chi) \\ \times p(\theta_1|\lambda_\theta)p(\theta_2|\lambda_\theta)p(z|\lambda_z)p(\Omega), \quad (16)$$

where $\lambda = \{\lambda_m, \lambda_z, \lambda_\chi, \lambda_\theta\}$. The symbol Ω collectively denotes all other parameters entering the GW approximant. Omitting some parameters in population inference is actually equivalent to assuming an astrophysical model where those parameters are distributed as in the Bayesian priors $p(\Omega)$ used in the underlying single-event analyses [18]. However, note that while the parameters Ω factor out in p_{pop} , they do enter the detectability function p_{det} .

We briefly summarize the population models used in this work as follows, see Table III. Appendix A provides a more detailed description of these models.

- *Mass distribution.* We use a slightly edited version of the popular POWER-LAW + PEAK model [5, 45, 46] with 9 free hyperparameters $\lambda_m = \{\alpha_m, \beta_q, \lambda_{\text{peak}}, \mu_m, \sigma_m, m_{\text{min}}, m_{\text{max}}, \sigma_1, \sigma_h\}$. The distribution of the primary mass m_1 is described by a power-law with slope $-\alpha_m$ extending between a minimum mass $m_{\text{min}} - \sigma_1$ and a maximum mass $m_{\text{max}} + \sigma_h$. A Gaussian feature is included to account for a possible concentration of events just close to the pair-instability supernova mass gap. This Gaussian peak is characterized by weight λ_{peak} , median μ_m , and standard deviation σ_m . The secondary mass m_2 is modeled by a power-law with spectral index β_q . The distributions of m_1 and

m_2 are smoothed over a range of masses σ_1 (σ_h) at the low (high) end of the mass function. Our smoothing prescription differ by that used elsewhere in the literature. In particular, we opted for polynomial smoothing functions for compatibility with the adopted automatic-differentiation strategy and numerical efficiency; see App. A.

- *Redshift distribution.* We use the so-called MADAU-DICKINSON profile [47] for the merger rate. This is parameterized by $\lambda_z = \{\alpha_z, \beta_z, z_p\}$, namely the redshift z_p at which the rate peaks and the power-law indices α_z and β_z that govern the rise and fall of rate at low and high redshifts, respectively.
- *Spin distribution.* The spin distribution is modeled after LIGO/Virgo's DEFAULT model where $\lambda_\chi = \{\alpha_\chi, \beta_\chi\}$ and $\lambda_\theta = \{\zeta, \sigma_t\}$ [5, 48]. The component spin magnitudes are independently drawn from a Beta distribution with shape parameters α_χ and β_χ . The distribution of the spin tilt cosines have a uniform component (describing dynamically formed binaries with isotropically oriented spins) and a truncated Gaussian component with mean 1, weight ζ and standard deviation σ_t (modeling BH binaries formed in isolated environment with preferentially aligned spins).

Unless stated otherwise, we adopt fiducial values for the mass and spin hyperparameters $\lambda_m, \lambda_\chi, \lambda_\theta$ using the medians of the marginalized distributions from GWTC-3 [5] and fiducial values of λ_z from Ref. [47]. In particular, we set $\alpha_m = 3.4, \beta_q = 1.1, m_{\text{min}} = 9.1 M_\odot, m_{\text{max}} = 87 M_\odot, \lambda_{\text{peak}} = 0.039, \mu_m = 34 M_\odot, \sigma_m = 3.6 M_\odot, \sigma_1 = 4 M_\odot, \sigma_h = 20 M_\odot, \alpha_z = 2.7, \beta_z = 3, z_p = 2, \alpha_\chi = 1.6, \beta_\chi = 4.12, \zeta = 0.66, \sigma_t = 1.5$. Note that our choice for the minimum mass $m_{\text{min}} = 9.1 M_\odot$ is different with respect to the median value of $\sim 5 M_\odot$ reported in Ref. [5]. This is because of the adopted smoothing function (see App. A). In our implementation one has that the population distribution function is zero for $m \leq m_{\text{min}} - \sigma_1$. As a result, our parameter m_{min} is shifted by σ_1 (which has fiducial value $4 M_\odot$) compared to that of Ref. [5].

C. Monte Carlo integrations and regularization

We approximate Eqs. (4) and (8–12) with Monte Carlo integration. In particular, we cast those expressions as

$$I(\bar{\lambda}) = \int X(\bar{\theta}, \bar{\lambda}) p_{\text{draw}}(\bar{\theta}) d\bar{\theta} \simeq \frac{1}{N_{\text{draw}}} \sum_i^{N_{\text{draw}}} X(\bar{\theta}_i, \bar{\lambda}), \quad (17)$$

where $\bar{\theta}_i \sim p_{\text{draw}}(\bar{\theta})$ and $X(\bar{\theta}, \bar{\lambda})$ is the ratio between the target distribution and $p_{\text{draw}}(\bar{\theta})$.

The injection distribution $p_{\text{draw}}(\bar{\theta})$ is chosen to improve convergence. For instance, it is convenient to use shallower power-laws (with spectral indexes closer to 0) to prevent undersampling in regions of the parameter space where

² These are available at apps.et-gw.eu/tds/?r=18213 and dcc.cosmicexplorer.org/CE-T2000017/public.

	ET		ET+2CE	
	σ_λ/λ [10^{-3}]	$T_{1\%}$ [yr]	σ_λ/λ [10^{-3}]	$T_{1\%}$ [yr]
α_m	1.5	0.2	1.3	0.2
β_q	7.1	5.1	6.6	4.3
λ_{peak}	5.8	3.4	5.4	2.9
μ_m	0.7	0.1	0.6	0.04
σ_m	5.7	3.3	5.2	2.7
m_{min}	1.1	0.1	0.9	0.1
m_{max}	15.7	>10	15.1	>10
σ_l	2.7	0.7	2.5	0.6
σ_h	10.3	>10	9.7	>10
α_z	6.7	4.5	5.9	1.4
β_z	5.6	3.1	3.8	0.2
z_p	4.7	2.2	3.7	1.4
α_χ	1.7	0.3	1.5	0.2
β_χ	1.8	0.3	1.5	0.2
ζ_χ	9.8	9.7	8.9	7.9
σ_t	5.3	2.8	5.1	2.6

Table I. Summary results from our fiducial model, see also Fig. 1. For ET and ET+2CE, we report relative errors σ_λ/λ after 10 years of observation as well as the required time to achieve a percent-level accuracy $\sigma_\lambda/\lambda = 1\%$. For readability, parameters are divided into four blocks (broad mass features, mass cutoffs, redshift, spins) as in Fig. 1.

$p_{\text{pop}}(\bar{\theta}|\bar{\lambda})$ is low but relevant for a specific element of $\bar{\lambda}$ (notably, this is the case of m_{max}). For the mass model, we use a draw population with $\alpha_m = \beta_q = 0.5$ and $\sigma_h = 20 M_\odot$. For all other hyperparameters, it is sufficient to draw samples using the true values $\bar{\lambda}$.

The subdominant terms $\Gamma_{\text{II-V}}$ depend on the single-event Fisher matrices Γ_θ evaluated at the draws $\bar{\theta}_i$. If some of these sources have low SNRs and/or are located at the edge of the parameter space, this might result in occasionally large numerical errors on Γ_θ , which in turn make the computation of Γ_λ numerically unstable. As a regularization strategy, we restrict the computation of the Monte Carlo sum in Eq. (17) to the inner 95% quantile of the evaluations $X(\bar{\theta}_i, \bar{\lambda})$. At least for the GWFAST implementation and using $N_{\text{draw}} = \mathcal{O}(10^5)$, this is sufficient to obtain stable results. For additional regularization purposes, we also set $p_{\text{pop}}(\theta|\lambda) = 0$ whenever this is $< 10^{-12}$. This helps avoiding numerical instabilities when taking derivatives with respect to the hyperparameters λ and we verified it does not affect our results in any meaningful way.

In the following, the number of significant digits used when presenting the results is determined by the variance of the adopted Monte Carlo estimators.

IV. RESULTS

We now present our results, starting from a broad overview and then exploring forecasts for mass, redshift, and spins in more details.

Figure 1 shows the relative errors σ_λ/λ of the 16 population hyperparameters as a function of the observation time for both the ET and ET+2CE configurations assuming our fiducial model. Results corresponding to $T_{\text{obs}} = 10$ yr are also reported in Table I, together with time required to achieve 1% accuracy in each of the hyperparameters. We divide our hyperparameters into four groups, separating those relative to broad mass features ($\alpha_m, \beta_q, \mu_m, \sigma_m, \lambda_{\text{peak}}$), mass cutoffs ($m_{\text{max}}, m_{\text{min}}, \sigma_h, \sigma_l$), redshift (z_p, α_z, β_z) and spins ($\alpha_\chi, \beta_\chi, \zeta, \sigma_t$). We consider a cumulative observation time $T_{\text{obs}} \in [0, 10]$ years and compute the corresponding number of detected events N_{det} as described in App. A. For our fiducial model, an observation time of 10 years corresponds to $\sim 5 \times 10^5$ ($\sim 7 \times 10^5$) detected events and a detection efficiency $p_{\text{det}}(\lambda) \simeq 69\%$ (96%) for ET (ET+2CE).

For the case of ET, Fig. 2 shows the joint distributions of the mass, spins, and redshift parameters, including their covariances. A similar plot where we compare (with caveats) against current results from LIGO/Virgo is presented in App. B. 3G detectors will be transformative, improving population constraints by orders of magnitudes.

We also present some variations around the fiducial model, changing in particular the maximum mass m_{max} , the peak of the redshift distribution z_p , and the aligned/isotropic mixing fraction ζ for the spin directions. These results are presented in Figs. 3, 4, 5, and Table II.

A. Detector networks

The most evident feature from Fig. 1 is the scaling

$$\frac{\sigma_\lambda}{\lambda} \propto \sigma_\lambda \propto \frac{1}{\sqrt{N}} \propto \frac{1}{\sqrt{N_{\text{det}}}} \propto \frac{1}{\sqrt{T_{\text{obs}}}}, \quad (18)$$

which is a direct consequence of Eqs. (4), (7), and (A8).

From Fig. 1 and Table I, we predict that the ET and ET+2CE will measure the population properties of BH binaries equally well, at least qualitatively. While there are small quantitative differences, the overall picture is very similar between the two cases. Adding additional 3G detectors to the network will not be crucial for measuring the intrinsic population properties of merging BHs. This result is largely expected, for a few reasons:

- (i) The overall scale of the problem is set by the number of detections. In the expressions above, this is indicated by the weight $p_{\text{det}}(\bar{\theta})p_{\text{pop}}(\bar{\theta}|\bar{\lambda})$ in the dominant Γ_1 integral of Eq. (8). For a given intrinsic number of events N (or equivalently T_{obs}), upgrading from ET to ET+2CE improves popula-

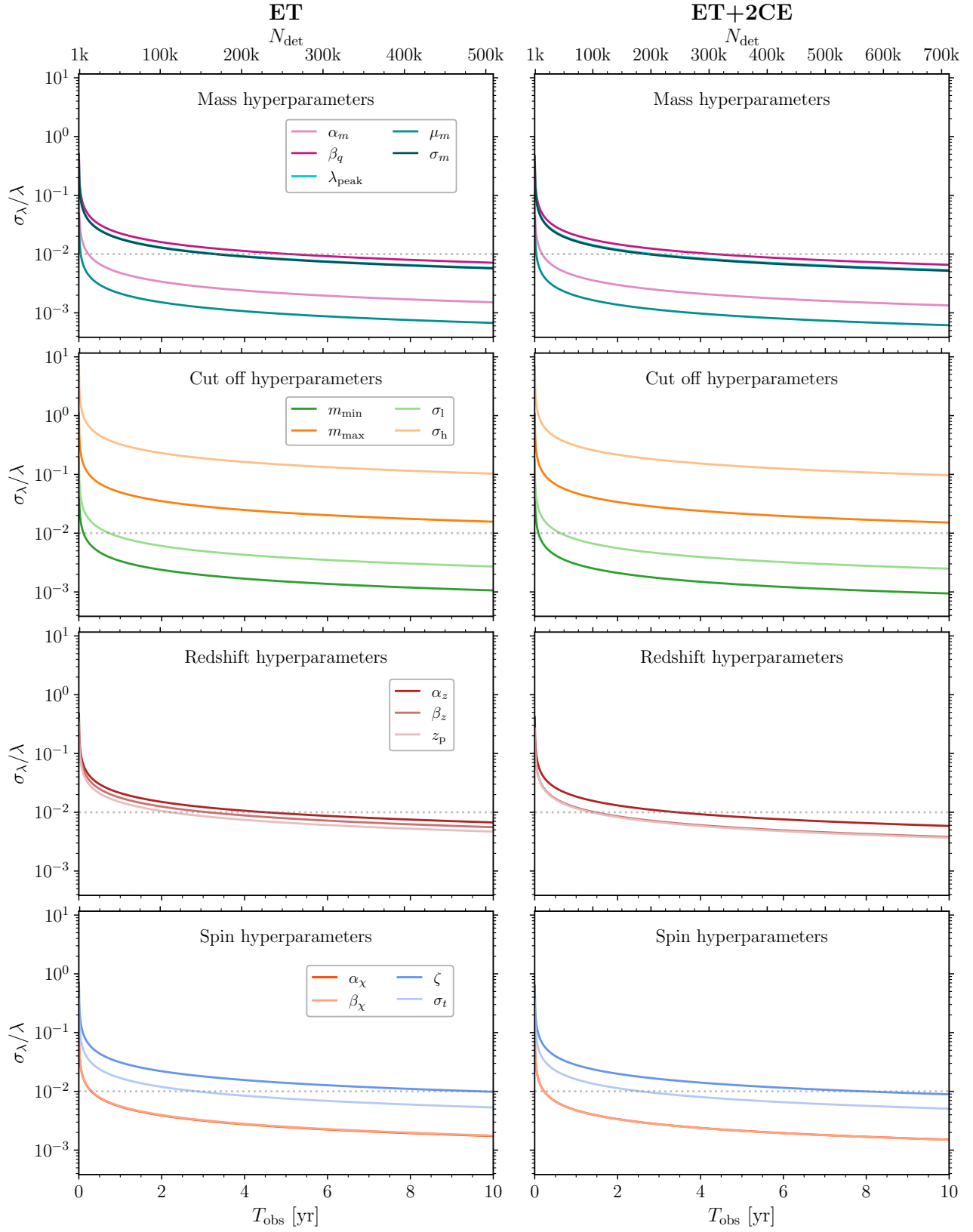


Figure 1. Relative errors of the model hyperparameters λ as a function of the observation time (bottom x -axis) for ET (left panels) and ET+2CE (right panels) assuming our fiducial population model. The upper x -axis indicates the corresponding number of detected events, which depends on the chosen detector network. The four rows correspond to the hyperparameters governing broad mass features, mass cutoffs, merger redshift evolution, and BH spins. To guide the eye, the dashed horizontal lines mark the threshold for percent-level accuracy, $\sigma_{\lambda}/\lambda = 1\%$. Some of these results are also reported in Table 1.

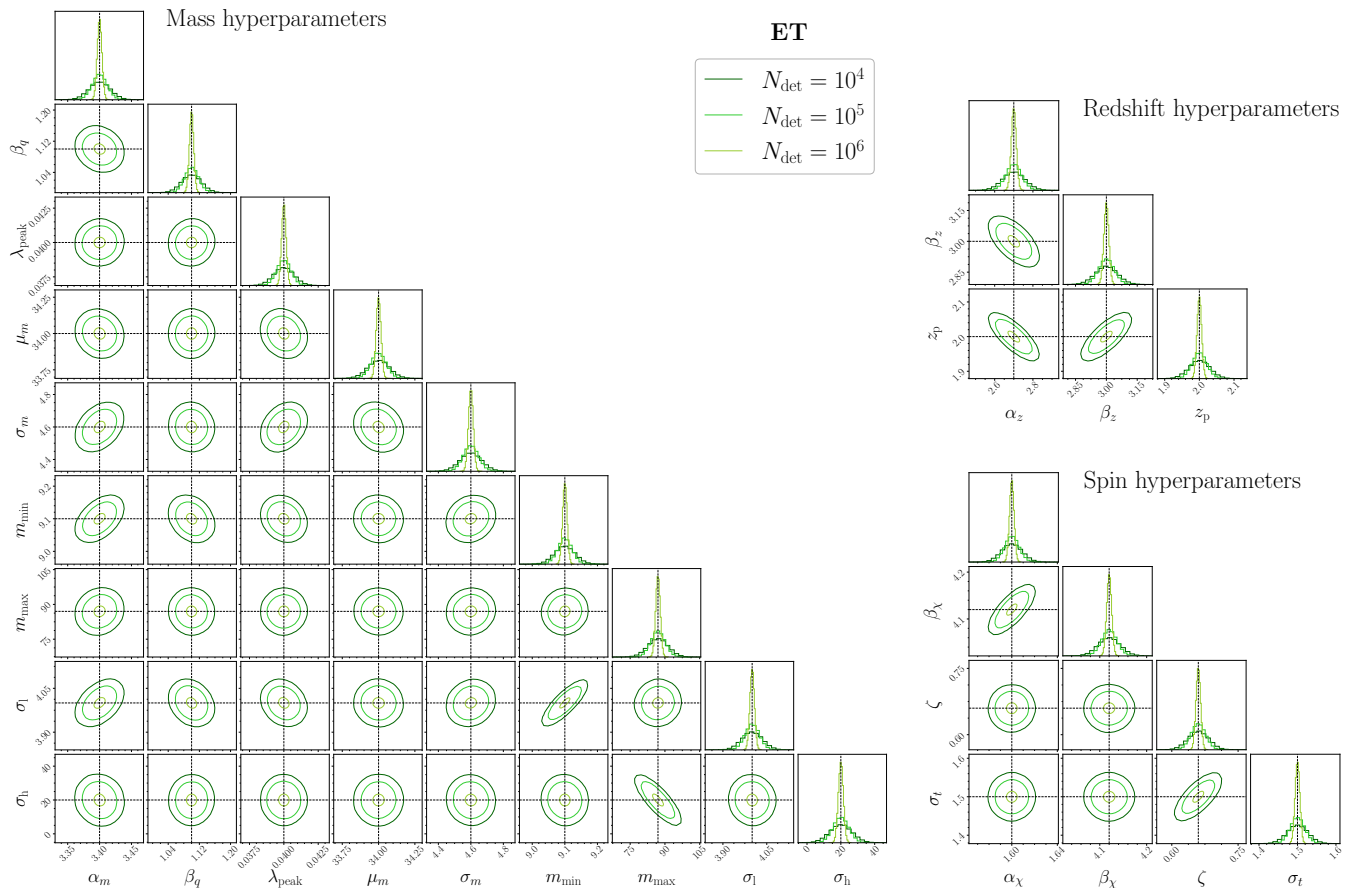


Figure 2. Hyperparameter uncertainties and their correlations assuming the ET detector and our fiducial population model. Contours indicate 90% credible intervals and black dashed lines indicate the injected values. We show results for catalogs of $N_{\text{det}} = 10^4, 10^5, 10^6$ events (darker to lighter) corresponding to $T_{\text{obs}} \simeq 0.2, 2, 19$ years.

tion constraints by as little as

$$1 - \sqrt{\frac{p_{\text{det,ET}}(\bar{\lambda})}{p_{\text{det,ET+2CE}}(\bar{\lambda})}} \sim 15\%. \quad (19)$$

This is only an approximate estimate because the detectable population $p_{\text{det}}(\bar{\theta})p_{\text{pop}}(\bar{\theta}|\bar{\lambda})$ is integrated over an additional derivative term in Eq. (8) and additional subdominant terms $\Gamma_{\text{II-V}}$ are present.

- (ii) While the individual-event measurement accuracies Γ_{θ} improve with multiple detectors, they enter the population Fisher matrix only through the subdominant terms $\Gamma_{\text{II-V}}$.
- (iii) In this work and as currently done in most of the literature (but see Ref. [49] for a notable exception) we only consider the population of masses, spins, and redshift. As is already the case for LIGO and Virgo, the accuracy of these parameters is largely dominated by the single most sensitive instrument in the network [1]. On the other hand, it is well known that expanding the network greatly pays off in terms of source localization.

- (iv) We restrict our study to the *global* population of sources and assume the BH merger rate roughly follows the star-formation rate, i.e. most of the events have $z \lesssim 2$. At these redshifts, the coverage provided by even a single ET instrument of triangular shape is essentially complete. This conclusion cannot be straightforwardly applied to putative subpopulations of sources at very high redshifts, e.g. those coming from population-3 stars [50] or primordial BHs [51]. While the ET+2CE network has a larger detection horizon compared to ET alone, detecting binaries at cosmological distances does not imply an accurate inference of their source parameters [52, 53].

B. Mass distribution

The primary mass distribution of binary BHs inferred from GWTC-3 spans from a few solar masses up to around $90 M_{\odot}$. It shows a power-law behavior, with a Gaussian component at $\sim 35 M_{\odot}$, which is below the pair-instability supernova mass gap that is predicted by

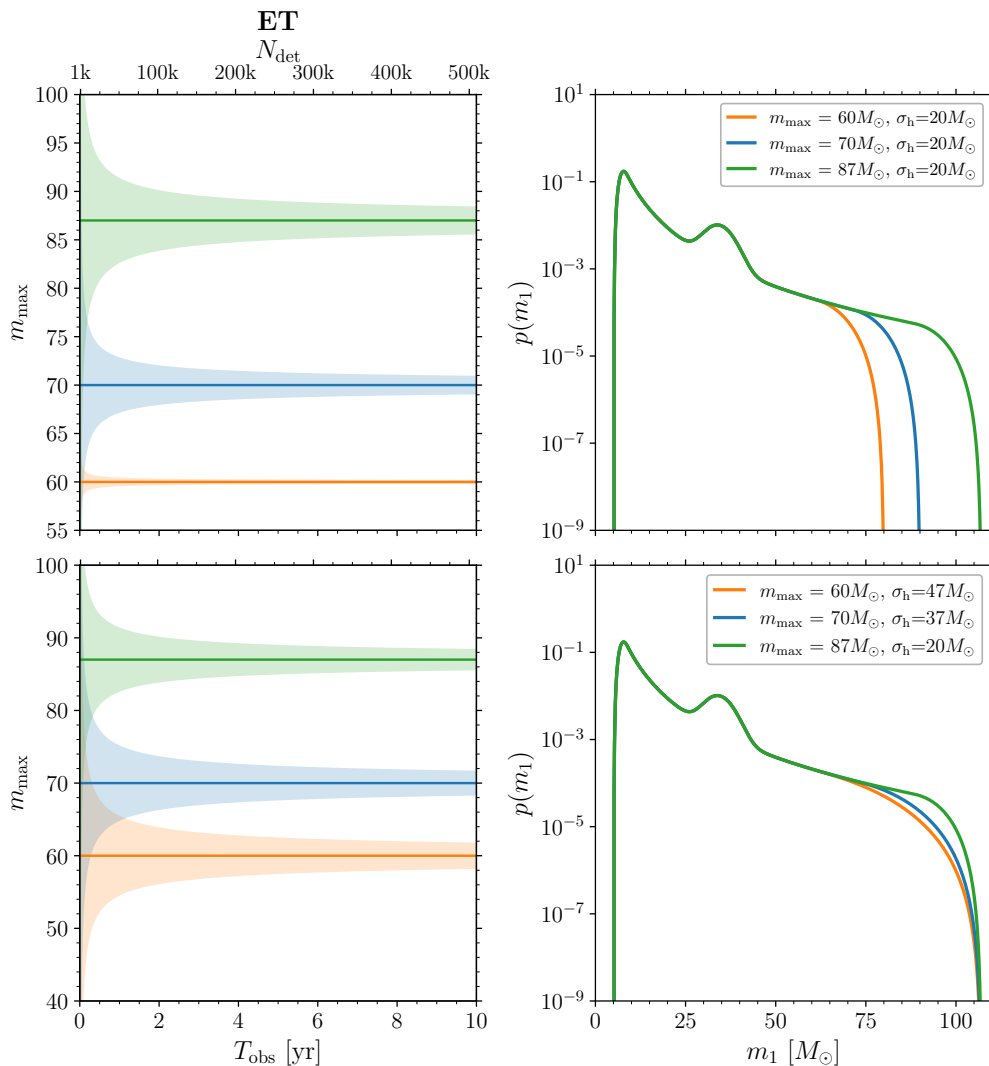


Figure 3. Measurability of upper edge of the mass spectrum as a function of the observation time T_{obs} (bottom x) axis for a single ET instrument. The corresponding number of detections is reported in the top x -axis. Top (bottom) panels show model variations around the fiducial model where we vary the maximum mass m_{max} and fix (vary) the related smoothing parameter σ_{h} . In both panels, the fiducial model is represented by the green curve with $m_{\text{max}} = 87 M_{\odot}$ and $\sigma_{\text{h}} = 20 M_{\odot}$. Left panels show the injected values (horizontal lines) and the related 1σ errors (shaded areas). For each model, the corresponding primary mass spectrum is illustrated in the right panels. Related results are presented in Table II.

stellar evolution models for BHs with masses in the range $\sim 40 - 120 M_{\odot}$ [54–57]. The astrophysical origin of this excess is uncertain. The primary mass spectrum reveals another notable peak at $\sim 10 M_{\odot}$, which has been suggested as an indicator of a significant contribution from isolated binary evolution [58–60]. The absence of a sharp cut-off for masses $\gtrsim 40 M_{\odot}$ might point to evolutionary paths in dynamical environments, including the occurrence of hierarchical mergers and/or formation in environments like galactic nuclei [8, 61, 62].

Figure 1 and Table I show that hyperparameters such as the minimum mass m_{min} , the spectral index α_m , and the position of the Gaussian peak μ_m in the primary mass spectrum are measured with high precision, reaching 1%

accuracy in just a few months of 3G operation. All of these are parameters that impact the population where the event rate is sufficiently large (i.e. close to the “top” of the underlying power-law structure). Measuring m_{min} will test the occurrence of the putative mass gap between BHs and neutron stars, measuring α_m will indicate whether the BH mass spectrum is shallower or steeper than that of stars, and measuring μ_m will delineate the boundary between BHs formed through supernova explosion and those potentially limited by pair instabilities, shedding light on the underlying physics of core collapse. The association of the Gaussian peak with the pulsational pair-instability mechanism remains uncertain, see e.g. Refs. [63, 64].

The secondary-mass spectral index β_q is measured less accurately than that of the primary mass α_m . This is due to both m_1 being easier to constrain than m_2 , but also to the specific functional form of $p_{\text{pop}}(\theta|\lambda)$ used here, which is written as two independent contributions $p(m_1)p(m_2|m_1)$.

In contrast, parameters such as the maximum mass m_{max} and the smoothing length σ_h are harder to measure because they affect the low-rate region of the population (at the “bottom” end of the underlying power-law). The accuracy of both these parameters does not go below 1% accuracy even after 10 years of 3G observations.

The corner plot of Fig. 2 shows that, as expected, the cutoff parameters at both the lower and upper ends of the mass spectrum exhibit distinct correlations with their respective smoothing hyperparameters. Specifically, the minimum mass m_{min} shows a positive correlation with σ_1 , indicating that an increase in m_{min} can be compensated by a simultaneous increase in σ_1 while still fitting the same population model. Conversely, the maximum mass m_{max} displays a negative correlation with σ_h ; thus, an increase in m_{max} necessitates a corresponding decrease in σ_h to maintain the same probability density function $p_{\text{pop}}(\theta|\lambda)$.

We also observe a positive correlation between m_{min} (and thus σ_1) and the spectral index α_m . This is because both a steeper power-law (larger α_m) and a more extended mass spectrum (lower m_{min}) predict a larger number of low-mass detections. We do not observe a similar correlation between α_m and m_{max} because there are significantly fewer events at the upper end of the mass spectrum. A similar but weaker behavior is observed also for the secondary-mass spectral index β_q .

The minimum mass m_{min} (and consequently σ_1) is also correlated with the fraction of sources in the Gaussian component λ_{peak} . As m_{min} and σ_1 increase, the contribution provided by the power-law component decreases (the power-law is “shorter”) and thus the weight of the Gaussian peak must increase. We further observe a negative correlation between the spectral indices α_m and β_q of the primary and secondary mass distribution, respectively. This can be understood as follows: a higher value for the primary mass spectral index, i.e. a steeper power-law, results in a larger number of light events, consequently flattening the secondary mass distribution, and thus lowering the value of β_q .

In Fig. 3 and Table II, we present two model variations to study the measurability of the upper cutoff m_{max} . The impact of these model variations on $p_{\text{det}}(\lambda)$ is of $\mathcal{O}(10^{-4})$, such that a given value of T_{obs} corresponds to GW catalogs of essentially the same size N_{det} .

- (i) First, we vary the maximum mass $m_{\text{max}} = 60 M_{\odot}, 70 M_{\odot}, 87 M_{\odot}$ while keeping all other hyperparameters fixed to their fiducial values, including the high-mass smoothing σ_h . We find that the uncertainties on the maximum mass increase with the value of the maximum mass itself. After $T_{\text{obs}} = 10$ years, ET will be able

	$\sigma_{\lambda} [10^{-2}]$		
	$m_{\text{max}} = 60 M_{\odot}$ $\sigma_h = 20 M_{\odot}$	$m_{\text{max}} = 70 M_{\odot}$ $\sigma_h = 20 M_{\odot}$	$m_{\text{max}} = 87 M_{\odot}$ $\sigma_h = 20 M_{\odot}$
α_m	0.28	0.25	0.51
β_q	0.71	0.80	0.78
λ_{peak}	0.02	0.02	0.02
μ_m	2.47	2.52	2.29
σ_m	2.49	2.99	2.05
m_{min}	1.02	0.95	0.97
m_{max}	11.59	87.80	136.23
σ_1	1.15	1.08	1.08
σ_h	11.77	131.20	205.65
	$m_{\text{max}} = 60 M_{\odot}$ $\sigma_h = 47 M_{\odot}$	$m_{\text{max}} = 70 M_{\odot}$ $\sigma_h = 37 M_{\odot}$	$m_{\text{max}} = 87 M_{\odot}$ $\sigma_h = 20 M_{\odot}$
α_m	0.56	0.54	0.51
β_q	0.82	0.81	0.78
λ_{peak}	0.02	0.02	0.02
μ_m	2.40	2.40	2.29
σ_m	2.15	2.14	2.05
m_{min}	0.94	0.93	0.97
m_{max}	169.90	160.62	136.23
σ_1	1.03	1.03	1.08
σ_h	264.31	245.29	205.65
	$z_p = 1$	$z_p = 2$	$z_p = 5$
α_z	3.32	1.81	0.92
β_z	1.35	1.67	2.95
z_p	0.70	0.94	1.78
	$\zeta = 0.1$	$\zeta = 0.66$	$\zeta = 1$
α_{χ}	0.27	0.28	0.28
β_{χ}	0.72	0.73	0.73
ζ	0.32	0.65	0.70
σ_t	20.95	7.99	5.62

Table II. Summary results from a few model variations. We show absolute errors σ_{λ} after 10 years of observation with ET. Starting from our fiducial model, we vary one or two parameters at a time. In particular, we explore variations of the maximum mass m_{max} (first block of cells), the maximum mass m_{max} and the smoothing parameter σ_h (second block of cells), the peak of the redshift distribution z_p (third block of cells), and the fraction of binaries with aligned spins ζ (fourth block of cell). The fiducial model corresponds to $m_{\text{max}} = 87 M_{\odot}$, $z_p = 2$, and $\zeta = 0.66$ as indicated in boldface. Related results are presented in Figs. 3, 4, 5.

to constrain the maximum mass with absolute errors of $\pm[1.159, 8.780, 13.623] \times 10^{-1} M_{\odot}$ for $m_{\text{max}} = [60, 70, 87] M_{\odot}$. Lowering the value of m_{max} shifts the cutoff closer to the region of the mass spectrum where the event rate is higher. Consequently, the greater density of observed events

provides more statistical information, allowing for more precise population constraints. A lower value of the maximum mass also decreases the errors on the smoothing parameter σ_h ; this might be due to the correlation between σ_h and m_{\max} highlighted above. The errors on the other mass hyperparameters remain approximately constant under these model variations.

- (ii) Second, we simultaneously vary the maximum mass $m_{\max} = 60 M_\odot, 70 M_\odot, 87 M_\odot$ and the smoothing length $\sigma_h = 47 M_\odot, 37 M_\odot, 20 M_\odot$ such that their sum $m_{\max} + \sigma_h = 107 M_\odot$ remains constant. Contrary to the previous case, here we find that errors on the maximum mass and that of the smoothing parameter σ_h decrease with the value of m_{\max} . In this controlled experiment, lower values of m_{\max} imply higher values of σ_h and thus a smoother high-mass end of the mass spectrum. Such prominent smoothing reduces the importance of the features near the cutoff, making it harder to pinpoint the exact location of m_{\max} . As a result, the uncertainty on both m_{\max} and σ_h increases with decreasing m_{\max} .

There is an important statistical caveat that affects some of the results we just described. Errors on broad features scale as the square root of the number of data-points, which is indeed the prediction of Eq. (18): $\sigma_\lambda \propto 1/\sqrt{N_{\text{det}}}$. This agrees with one’s intuition from the central limit theorem. However, the case of cutoff parameters is different and, instead, errors are expected to scale as $1/N_{\text{det}}$ (this is the popular “German tank” problem in statistics [65]). This property is not captured by the Fisher matrix formalism, which expands the likelihood around the true value λ — an expansion that should not be allowed at the edge of a distribution. While mitigated by the smoothing parameters σ_h and σ_l , this caveat affects our Fisher-based error estimates of m_{\min} and m_{\max} . Our results are therefore conservative: we predict a $1/\sqrt{T_{\text{obs}}}$ scaling but this could actually be as rapid as $1/T_{\text{obs}}$. This same feature was already noted in single-event parameter estimation when experimenting with truncated waveforms [66].

C. Redshift distribution

Current GW data provide conclusive evidence that the BH merger rate evolves with redshift. Assuming the merger rate evolves as $R(z) = R_0(1+z)^\kappa$, GWTC-3 data indicate $\kappa \sim 3$ [5], which is consistent with the rise of the star-formation rate with redshift in the local Universe [67–70]. Modeling the evolution of the merger rate with redshift using a single power-law is not appropriate for 3G detectors because their detection horizon extends far beyond the peak of the star-formation rate. This is indeed the key reason behind choosing the MADAU–DICKINSON profile instead, cf. Sec. III B.

The third row of Fig. 1 illustrates the relative errors on the redshift hyperparameters for the fiducial model,

assuming either ET or ET+2CE. Again, we report qualitatively similar performances for both detector configurations. However, when compared to masses and spins, the redshift distribution is more prominently affected by the expansion of the detector network. This is because a network of well-separated interferometers has better sky localization capabilities, thus breaking the known degeneracy with the distance to the source, and thus with the redshift (let us recall that here we are fixing the cosmology). Improvements saturate as T_{obs} increases and marginal gains require longer times. For our fiducial model, we find that all parameters associated with the redshift evolution achieve 1% accuracy within a range of 2 months to 1.5 years when using ET+2CE, whereas the single ET configuration requires 2 to 4.5 years (Table I).

Figure 2 shows that all the redshift hyperparameters are tightly correlated. In particular, there is a positive (negative) correlation between β_z (α_z) and the peak of the merger rate z_p . This is largely because we are keeping the local merger rate R_0 fixed. If the redshift peak is higher, the merger rate must be steeper at high redshift and shallower at low redshift.

Finally, Fig. 4 shows a model-variation study where we shift the peak of the redshift distribution $z_p = 1, 2, 5$, considering a single ET instrument. We find that the errors decrease with increasing z_p , which is once more a direct consequence of our rate choice. Fixing the local rate R_0 implies that these different models refer to Universes with a different number of BH mergers N (and thus a different number of detected events N_{det}); cf. App. A 2. In this context, assuming a model with a large value of z_p corresponds to assuming more merging BHs, which in turn results in better population constraints. An alternative choice would be to fix the total merger rate instead of the local value R_0 .

D. Spin distribution

As for the spin distribution, current GW data reveals evidence of both aligned and misaligned spins. Systems with large spin-orbit misalignment suggest formation in dynamically active environments like globular clusters or AGN disks, where interactions can randomize spin directions; on the other hand, aligned spins suggest formation from isolated binary stars [48, 71–73]. The BH spin magnitudes contain information on the details of stellar collapse including the efficiency of angular momentum transfer between stellar cores and envelopes as well as the occurrence of previous mergers [59, 74–76].

Figure 1 and Table I show that, among the spin hyperparameters, those with tighter constraints are the shape parameters entering the Beta distribution of the spin magnitudes. Both ET and ET+2CE achieve percent-level accuracy for α_χ and β_χ after just a few months of operation. In contrast, the hyperparameters associated with the spin orientations exhibit much longer timescales to reach similar accuracy levels. In particular, the mixing

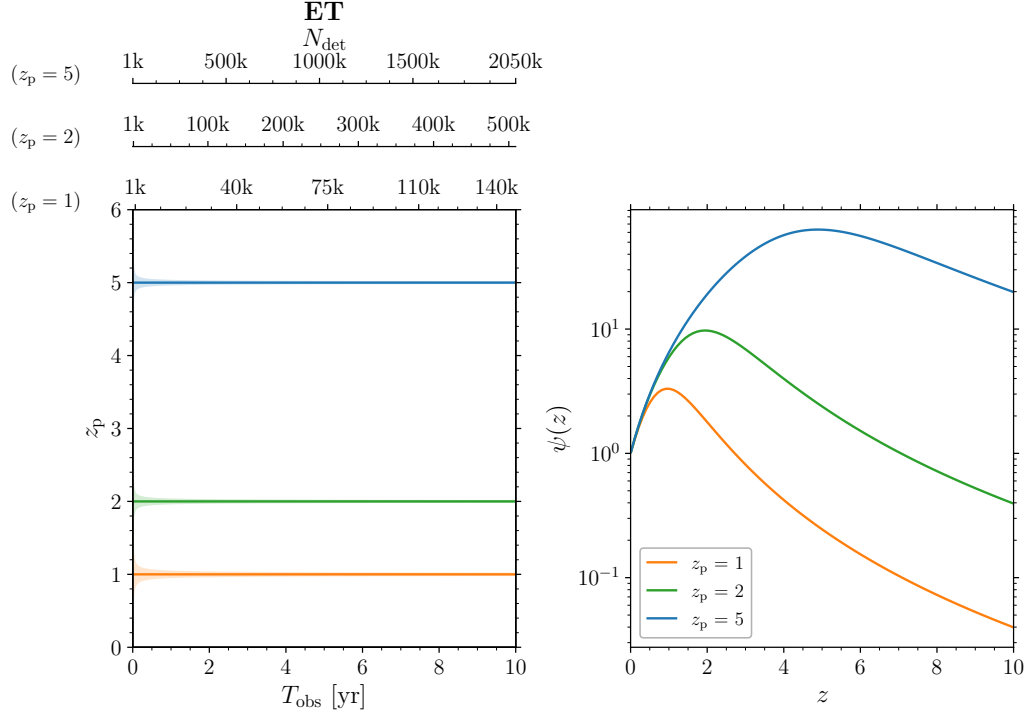


Figure 4. Measurability of the redshift at which the merger rate is maximum z_p as a function of the observation time T_{obs} (bottom x -axis) for a single ET instrument. We consider three models with $z_p = 1, 2,$ and 5 ; the three top x -axes show the corresponding number of detected events N_{det} . The fiducial model is represented by the green curve with $z_p = 2$. The left panel show the injected values (horizontal lines) and the related 1σ errors (shaded areas). For each model, the corresponding merger rate $\psi(z)$ is illustrated in the right panels; this is normalized such that $\psi(z = 0) = 1$. Related results are presented in Table II.

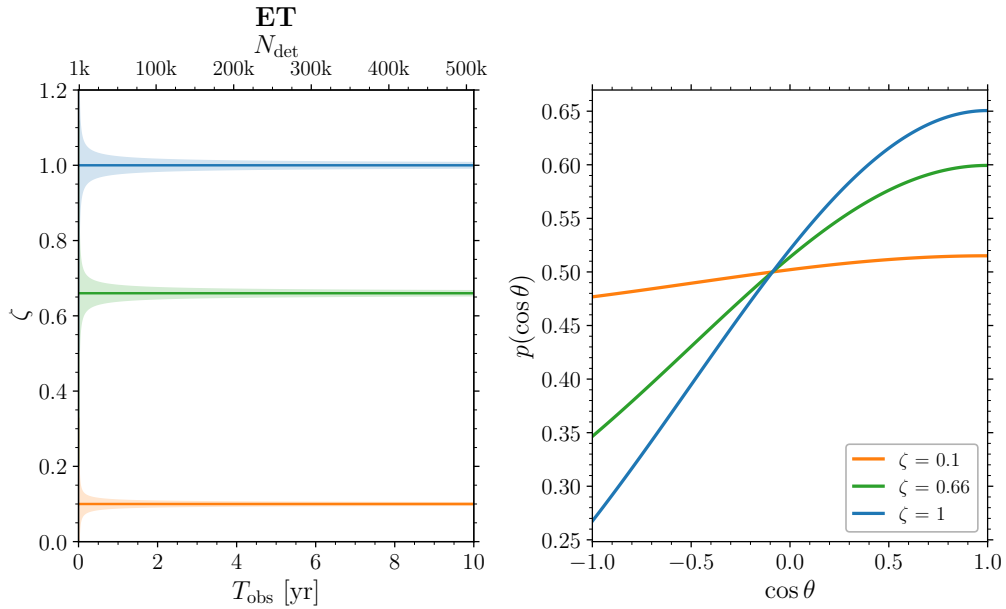


Figure 5. Measurability of the mixing fraction ζ between BH binaries with aligned and misaligned spins as a function of the observation time T_{obs} (bottom x -axis) for a single ET instrument. The corresponding number of detections is reported in the top x -axis. We consider three model variations with $\zeta = 0.1, 0.66,$ and 1 . The fiducial model is represented by the green curve with $\zeta = 0.66$. The left panel shows the injected values (horizontal lines) and the related 1σ errors (shaded areas). For each model, the corresponding distribution of the spin-orbit angle is illustrated in the right panels. Related results are presented in Table II.

fraction ζ requires nearly 10 years of observations for both configurations to achieve an accuracy of 1%. Note that, for the spin case, the population Fisher terms $\Gamma_{\text{II-V}}$ become almost comparable to Γ_{I} , meaning that the single event errors on the spins are no longer irrelevant for the population analysis.

Our results suggest that the broad program of pinpointing the BH binary formation channel using the spin orientations will face some serious challenges, even in the 3G era. A crucial element on this point will be the achieved low-frequency sensitivity of ET and CE. For the noise curves used here, we have $f \gtrsim 2$ Hz for ET and $f \gtrsim 5$ Hz for CE. Pushing the low-frequency requirement will allow the inspiral phase, where spins are prominent observables, to be better resolved, which impacts both accuracies and event rates.

The corner plot in Fig. 2 shows that the hyperparameters modeling the spin magnitudes and those modeling the spin directions are respectively correlated within their own groups. In particular, we find a positive correlation in both $(\alpha_\chi - \beta_\chi)$ and $(\zeta - \sigma_t)$. We do not observe any meaningful cross-correlations between hyperparameters modeling the spin magnitudes and those modeling the spin orientations, which is expected being the two distributions independent.

Finally, in Fig. 5 we study the measurability of the relative weight of the isotropic ($\zeta = 0$) and aligned ($\zeta = 1$) component of the spin-direction population, which is meant to capture the fraction of systems originating from dynamical and isolated channels [48]. We vary $\zeta = 0.1, 0.66, 1$ while keeping all other hyperparameters fixed to their fiducial values. Table II shows that varying ζ does not influence the absolute errors on either α_χ or β_χ (which agrees with the statement above about these parameters being largely uncorrelated). On the other hand, we observe that the error on σ_t raises (lowers) for smaller (larger) values of ζ . This can be traced to the fact that larger values for ζ predict more events in the Gaussian component, which is then easier to characterize. Finally, we find that the absolute uncertainty on ζ diminishes for lower values of this hyperparameter. As previously remarked, for the spin case single-event parameter reconstruction is found to be relevant through the terms $\Gamma_{\text{II-V}}$. For lower values of ζ a larger fraction of the events have precessing spins, in which case tilt angles are easier to reconstruct as compared to $\theta_i \sim \pm\pi/2$.

V. CONCLUSIONS

We presented a Fisher-matrix implementation to forecast the population properties of merging BH binaries detectable by 3G observatories such as ET and CE. The starting point of this paper is the formalism developed by Gair *et al.* [34]. Our results show that future detectors will improve the precision with which we can constrain the population of compact binaries by orders of magnitude compared to LIGO/Virgo, with error bars on the

hyperparameters tightening at a rate $\propto 1/\sqrt{T_{\text{obs}}}$. This is actually a conservative estimate, as some of the edge parameters could actually improve as fast as $1/T_{\text{obs}}$ (the so-called ‘‘German tank’’ problem [65]).

While prospects are exciting, our analysis also reveals that, at least when modeling the population of masses, spins, and redshift, a single ET instrument of triangular shape and a network of ET and two CE’s will return qualitatively similar constraints. We expect similar conclusions to hold true also in the case of two L-shaped ET detectors [2]. This point is worth investigating more thoroughly.

We predict that some of the key mass-related hyperparameters, such as the minimum BH mass m_{min} and the spectral index of the primary mass distribution α_m can reach sub-percent accuracy within a few years of observation. The best-measured hyperparameter is μ_m , i.e. the position of the Gaussian peak. This is particularly promising, showing that 3G detectors will be able to deliver precision science on localized features in the population of merging compact objects. On the other hand, we predict that the upper edge of the primary mass spectrum m_{max} as well as the fraction of binaries with aligned vs misaligned spins are significantly harder to measure, reaching an accuracy of 1% only after $\gtrsim 8$ years of operations and several hundreds of thousands of events. This questions the feasibility of their related science case, namely pair-instability physics and formation channels, respectively.

We hope this paper will move the signpost from individual events to populations of events in the context of 3G-detector forecasts. This is particularly timely given the current planning activities regarding the construction of such facilities. Beside 3G detectors, our tool could also be useful for current LIGO/Virgo analyses where, even though this Fisher approach is unreliable, it could provide some intuition about the response of specific parametric population models.

Our implementation is built on top of the GWFAST code ³ [26] and will be made publicly available in due course ⁴. While state-of-the-art for LIGO/Virgo and $\mathcal{O}(100)$ events, the population models implemented here are admittedly too simple for 3G detectors, where the much larger statistics will allow probing far more features in the compact-binary population. Third-generation detectors will reveal detailed population structures, which will need to be matched by more flexible population models. Developing forecasts in this direction is left to future work.

³ <https://github.com/CosmoStatGW/gwfast>

⁴ <https://github.com/CosmoStatGW/gwfast/tree/master/gwfast/population>

ACKNOWLEDGMENTS

We thank Andrea Antonelli, Ssohrab Borhanian, Rodrigo Tenorio, Arianna Renzini, Christopher Moore, and Konstantin Leyde for discussions. V.D.R., D.G., and C.P. are supported by ERC Starting Grant No. 945155–GWmining, Cariplo Foundation Grant No. 2021-0555, MUR PRIN Grant No. 2022-Z9X4XS, MUR Grant “Progetto Dipartimenti di Eccellenza 2023-2027” (BiCoQ), and the ICSC National Research Centre funded by NextGenerationEU. V.D.R. is supported by an “Exchange Extra-EU” scholarship of the University of Milano-Bicocca. F.I. is supported by Swiss National Science Foundation, Grant No. 200020_191957 and the SwissMap National Center for Competence in Research. D.G. is supported by MSCA Fellowships No. 101064542–StochRewind and No. 101149270–ProtoBH. M.M. and V.D.R. supported by the French government under the France 2030 investment plan, as part of the Initiative d’Excellence d’Aix-Marseille Université – A*MIDEX AMX-22-CEI-02. Computational work was performed at CINECA with allocations through INFN and Bicocca.

Appendix A: Details of the population models

In this appendix we provide details about the parameterized population models used in this paper; a concise list of the relevant hyperparameters is provided in Table III together with the adopted fiducial values. We stress that, while here we describe only the adopted models, the developed code can trivially be extended to implement different distributions.

1. Mass population model

For the BH masses we adopt the POWER-LAW+PEAK model first introduced in [4]. The primary (heavier) object is distributed according to

$$p(m_1|\lambda_m) \propto [(1-\lambda_{\text{peak}}) \times \mathcal{P}(m_1|-\alpha_m, m_{\min}-\sigma_1, m_{\max}+\sigma_h) + \lambda_{\text{peak}}\mathcal{N}(m_1|\mu_m, \sigma_m)] \mathcal{S}(m_1|m_{\min}-\sigma_1, \sigma_1) \times [1 - \mathcal{S}(m_1|m_{\max}, \sigma_h)], \quad (\text{A1})$$

where $\mathcal{P}(m_1|-\alpha_m, m_{\min}-\sigma_1, m_{\max}+\sigma_h)$ is a power-law distribution with spectral index $-\alpha_m$ normalized in the interval $[m_{\min}-\sigma_1, m_{\max}+\sigma_h]$, $\mathcal{N}(m_1|\mu_m, \sigma_m)$ is a normalized Gaussian distribution with mean μ_m and standard deviation σ_m . For the smoothing functions \mathcal{S} , we design and employ a different prescription compared to that of Ref. [4, 5]. The specific functional form of their smoothing is numerically challenging to treat with automatic differentiation. We also note that their functions only *tend* to zero, without actually reaching the limit value. We use the following polynomial filter, which smoothly evolves

from 0 to 1 with vanishing first and second derivatives at the edges:

$$\mathcal{S}(x|x_0, \sigma_x) = \begin{cases} 0 & x < x_0, \\ f(x|x_0, \sigma_x) & x_0 \leq x \leq x_0 + \sigma_x, \\ 1 & x > x_0 + \sigma_x, \end{cases} \quad (\text{A2})$$

$$f(x|x_0, \sigma_x) = \frac{(x-x_0)^3}{\sigma_x^5} [10\sigma_x^2 - 15\sigma_x(x-x_0) + 6(x-x_0)^2], \quad (\text{A3})$$

where x_0 represents the lower edge, below which the filter vanishes, and σ_x controls the width of the transition. The above definition of the filter makes our implementation numerically stable when computing derivatives, and further allows to analytically compute the normalization of the chosen mass distribution, resulting in a faster numerical evaluation. Within our setting, the filtered mass distribution vanishes at $m_{\min}-\sigma_1$ and at $m_{\max}+\sigma_h$, with the onset of the filtering being at m_{\min} and m_{\max} .

As for the mass of the secondary object, the distribution is given by a power-law with the modified smoothing function described above

$$p(m_2|\lambda_m, m_1) \propto \mathcal{P}(m_2|\beta_q, m_{\min}-\sigma_1, m_1) \times \mathcal{S}(m_2|m_{\min}-\sigma_1, \sigma_1) \times [1 - \mathcal{S}(m_2|m_{\max}, \sigma_h)], \quad (\text{A4})$$

which is then normalized (again analytically) in the interval $[m_{\min}-\sigma_1, m_1]$ depending on m_1 , ensuring that $\int p(m_1, m_2|\lambda_m) dm_2 = p(m_1|\lambda_m)$.

2. Redshift population model

We assume that the merger rate only depends on the redshift z , i.e.

$$\frac{dN}{dt_s dV_c} = R_0 \psi(z|\lambda_z), \quad (\text{A5})$$

where N is the number of mergers (not the number of detections, see below), t_s is the source-frame time, V_c is the comoving volume, is R_0 the local merger rate at $z=0$, and $\psi(z)$ is a function such that $\psi(z=0)=1$. For the latter, we adopt the Madau-Dickinson profile [47], which has the following functional form [77]

$$\psi(z|\lambda_z) = \frac{[(1+z_p)^{\alpha_z+\beta_z} + 1](1+z)^{\alpha_z}}{(1+z_p)^{\alpha_z+\beta_z} + (1+z)^{\alpha_z+\beta_z}}, \quad (\text{A6})$$

where α_z (β_z) model the rise (decline) of the function at low (high) redshift, and z_p models the peak of the merger rate. The redshift distribution of the events is then given by [45, 78]

$$p(z|\lambda_z) \propto \psi(z|\lambda_z) \frac{dV_c}{dz} \frac{1}{1+z}. \quad (\text{A7})$$

Parameter	Description	Fiducial
λ_m	Mass model: POWER-LAW PLUS PEAK	
α_m	Spectral index for the power-law of the primary mass distribution.	3.4
m_{\min}	Minimum mass of the power-law component of the primary mass distribution.	$9.1 M_{\odot}$
m_{\max}	Maximum mass of the power-law component of the primary mass distribution.	$87 M_{\odot}$
λ_{peak}	Fraction of binary BHs in the Gaussian component.	0.039
μ_m	Mean of the Gaussian component in the primary mass distribution.	34
σ_m	Width of the Gaussian component in the primary mass distribution.	3.6
β_q	Spectral index for the power-law of the secondary mass distribution.	1.1
σ_1	Width of mass smoothing at the lower end of the mass distribution.	4.0
σ_h	Width of mass smoothing at the upper end of the mass distribution.	0.5
λ_z	Redshift model: MADAU-DICKINSON	
α_z	Power-law index governing the rise of the merger rate at low redshift.	2.7
β_z	Power-law index governing the decline of the merger rate at high redshift.	3.0
z_p	Redshift at which the merger rate peaks.	2.0
$\lambda_{\chi}, \lambda_{\theta}$	Spin model: DEFAULT	
α_{χ}	Mean of the Beta distribution of the spin magnitudes.	1.6
β_{χ}	Standard deviation of the Beta distribution of the spin magnitudes.	4.12
ζ	Mixing fraction of mergers from the truncated Gaussian component for spin orientations.	0.66
σ_t	Width of the truncated Gaussian component for spin orientations.	1.5

Table III. Summary of the population model parameters and their fiducial values.

The total number of mergers is given by

$$\begin{aligned}
 N &= \int \frac{dN}{dt_s dV_c} \frac{dV_c}{dz} \frac{dt_s}{dt_d} dz dt_d \\
 &= T_{\text{obs}} R_0 \int_0^{\infty} \psi(z|\lambda_z) \frac{1}{1+z} \frac{dV_c}{dz} dz, \quad (\text{A8})
 \end{aligned}$$

where t_d is the time at the detector, $dt_s/dt_d = 1/(1+z)$, and $\int dt_d = T_{\text{obs}}$ is the data taking period. In Sec. IV, we use the expressions above to estimate the time T_{obs} needed to observe a given number of detected events N_{det} . In particular, we compute N using Eq. (A8) and then approximate $N_{\text{det}} \simeq N p_{\text{det}}(\lambda)$, neglecting the expected Poisson fluctuation in the number of observed events.

In this paper, we fix the local merger rate to $R_0 = 17 \text{ Gpc}^{-3} \text{ yr}^{-1}$ [5]; computing the Fisher-matrix error on R_0 is a natural extension of this paper and requires generalizing Eq. (3) to the non-marginalized population likelihood (see App. A of Ref. [34]).

3. Spin population model

For the spins we again follow [4, 5] and adopt their DEFAULT model. This features a Beta distribution for the (independent) spin magnitudes

$$p(\chi_i|\lambda_{\chi}) = \text{Beta}(\chi_i|\alpha_{\chi}, \beta_{\chi}), \quad i = \{1, 2\}, \quad (\text{A9})$$

where α_{χ} and β_{χ} are the shape parameters for the distribution. These can be converted into mean and variance,

which are used in some of the GW literature to characterize the spin distribution.

The angles θ_i between each spin and the orbital angular momentum of the binary are drawn (again independently) from

$$p(\cos \theta_i|\lambda_{\theta}) = \zeta \mathcal{N}_{\text{tr}}(\cos \theta_i|1, \sigma_t) + (1-\zeta) \mathcal{I}(\cos \theta_i), \quad (\text{A10})$$

where $\mathcal{N}_{\text{tr}}(\cos \theta_i|1, \sigma_t)$ denotes a truncated Gaussian distribution between $[-1, 1]$ centered on 1 and with standard deviation σ_t , and $\mathcal{I}(\cos \theta_i)$ denotes an isotropic distribution in $[-1, 1]$.

Appendix B: LIGO/Virgo vs 3G

In Fig. 6 we compare our results against those obtained with current LIGO/Virgo data. For concreteness, we consider our fiducial model and ET with $N_{\text{det}} = 10^5$ ($T_{\text{obs}} \simeq 2 \text{ yr}$). We use public LIGO/Virgo/KAGRA data products from GWTC-3 [5], selecting data from their POWER-LAW PLUS PEAK mass distribution, DEFAULT spin model, and POWER-LAW redshift model.

While indicative, there are important caveats to this comparison. As discussed in App. A 1, the smoothing function we adopt differs from that of Ref. [5]. First, we smooth both the lower and upper ends of the mass spectrum while they only smooth the lower end. The parameters σ_h and σ_1 have different meanings in the two cases, and are thus omitted from Fig. 6. Moreover, while in our case the mass distribution vanishes at $m \leq m_{\min} - \sigma_1$, in

the prescription used by LIGO/Virgo/KAGRA it instead vanishes at $m \leq m_{\min}$. For a fairer comparison, we artificially shift the GWTC-3 m_{\min} posterior by $\sigma_1 = 4 M_{\odot}$. As for the redshift distribution, the POWER-LAW model

used in Ref. [5] is described by a single hyperparameter κ , that can only be approximately compared to α_z from the MADAU-DICKINSON model.

-
- [1] B. P. Abbott, R. Abbott, T. D. Abbott, M. R. Abernathy, F. Acernese, K. Ackley, C. Adams, T. Adams, P. Addesso, R. X. Adhikari, and et al., *Living Rev. Relativ.* **21**, 3 (2018), arXiv:1304.0670 [gr-qc].
- [2] M. Branchesi, M. Maggiore, et al., *J. Cosmology Astropart. Phys.* **2023**, 068 (2023), arXiv:2303.15923 [gr-qc].
- [3] B. P. Abbott et al., *Astrophys. J. Lett.* **882**, L24 (2019), arXiv:1811.12940 [astro-ph.HE].
- [4] R. Abbott et al., *Astrophys. J. Lett.* **913**, L7 (2021), arXiv:2010.14533 [astro-ph.HE].
- [5] R. Abbott et al., *Phys. Rev. X* **13**, 011048 (2023), arXiv:2111.03634 [astro-ph.HE].
- [6] I. Mandel and A. Farmer, *Phys. Rep.* **955**, 1 (2022), arXiv:1806.05820 [astro-ph.HE].
- [7] M. Mapelli, in *Handbook of Gravitational Wave Astronomy* (Springer, Singapore, 2021) p. 16.
- [8] D. Gerosa and M. Fishbach, *Nat. Astron.* **5**, 749 (2021), arXiv:2105.03439 [astro-ph.HE].
- [9] T. A. Callister, C.-J. Haster, K. K. Y. Ng, S. Vitale, and W. M. Farr, *Astrophys. J. Lett.* **922**, L5 (2021), arXiv:2106.00521 [astro-ph.HE].
- [10] C. Adamcewicz and E. Thrane, *Mon. Not. R. Astron. Soc.* **517**, 3928 (2022), arXiv:2208.03405 [astro-ph.HE].
- [11] C. Adamcewicz, P. D. Lasky, and E. Thrane, *Astrophys. J.* **958**, 13 (2023), arXiv:2307.15278 [astro-ph.HE].
- [12] S. Biscoveanu, T. A. Callister, C.-J. Haster, K. K. Y. Ng, S. Vitale, and W. M. Farr, *Astrophys. J. Lett.* **932**, L19 (2022), arXiv:2204.01578 [astro-ph.HE].
- [13] J. Heinzl, S. Vitale, and S. Biscoveanu, *Phys. Rev. D* **109**, 103006 (2024), arXiv:2312.00993 [astro-ph.HE].
- [14] S. Rinaldi, W. Del Pozzo, M. Mapelli, A. Lorenzo-Medina, and T. Dent, *Astron. Astrophys.* **684**, A204 (2024), arXiv:2310.03074 [astro-ph.HE].
- [15] G. Pierra, S. Mastrogiovanni, and S. Perriès, (2024), arXiv:2406.01679 [gr-qc].
- [16] J. Heinzl, M. Mould, and S. Vitale, (2024), arXiv:2406.16844 [astro-ph.HE].
- [17] I. Mandel, W. M. Farr, and J. R. Gair, *Mon. Not. R. Astron. Soc.* **486**, 1086 (2019), arXiv:1809.02063 [physics.data-an].
- [18] S. Vitale, D. Gerosa, W. M. Farr, and S. R. Taylor, in *Handbook of Gravitational Wave Astronomy* (Springer, Singapore, 2022) p. 45.
- [19] V. Tiwari, *Class. Quantum Grav.* **35**, 145009 (2018), arXiv:1712.00482 [astro-ph.HE].
- [20] W. M. Farr, *Res. Notes AAS* **3**, 66 (2019), arXiv:1904.10879 [astro-ph.IM].
- [21] C. Talbot and J. Golomb, *Mon. Not. R. Astron. Soc.* **526**, 3495 (2023), arXiv:2304.06138 [astro-ph.IM].
- [22] M. Punturo et al., *Class. Quantum Grav.* **27**, 194002 (2010).
- [23] D. Reitze et al., *Bull. Am. Astron. Soc.* **51**, 35 (2019), arXiv:1907.04833 [astro-ph.IM].
- [24] F. Iacovelli, M. Mancarella, S. Foffa, and M. Maggiore, *Astrophys. J.* **941**, 208 (2022), arXiv:2207.02771 [gr-qc].
- [25] M. Vallisneri, *Phys. Rev. D* **77**, 042001 (2008), arXiv:gr-qc/0703086 [gr-qc].
- [26] F. Iacovelli, M. Mancarella, S. Foffa, and M. Maggiore, *Astrophys. J. Supp. S.* **263**, 2 (2022), arXiv:2207.06910 [astro-ph.IM].
- [27] S. Borhanian, *Class. Quantum Grav.* **38**, 175014 (2021), arXiv:2010.15202 [gr-qc].
- [28] U. Dupletsa, J. Harms, B. Banerjee, M. Branchesi, B. Goncharov, A. Maselli, A. C. S. Oliveira, S. Ronchini, and J. Tissino, *Astron. Comput.* **42**, 100671 (2023), arXiv:2205.02499 [gr-qc].
- [29] Y. Li, I. S. Heng, M. L. Chan, C. Messenger, and X. Fan, *Phys. Rev. D* **105**, 043010 (2022), arXiv:2109.07389 [astro-ph.IM].
- [30] M. Pieroni, A. Ricciardone, and E. Barausse, *Sci. Rep.* **12**, 17940 (2022), arXiv:2203.12586 [astro-ph.CO].
- [31] B. P. Abbott, R. Abbott, T. D. Abbott, M. R. Abernathy, K. Ackley, C. Adams, P. Addesso, R. X. Adhikari, V. B. Adya, C. Affeldt, and et al., *Class. Quantum Grav.* **34**, 044001 (2017), arXiv:1607.08697 [astro-ph.IM].
- [32] M. Maggiore, C. Van Den Broeck, et al., *J. Cosmology Astropart. Phys.* **2020**, 050 (2020), arXiv:1912.02622 [astro-ph.CO].
- [33] M. Evans et al., (2021), arXiv:2109.09882 [astro-ph.IM].
- [34] J. R. Gair, A. Antonelli, and R. Barbieri, *Mon. Not. R. Astron. Soc.* **519**, 2736 (2023), arXiv:2205.07893 [gr-qc].
- [35] M. Maggiore, *Gravitational Waves. Vol. 1: Theory and Experiments* (Oxford, 2007).
- [36] E. Pizzati, S. Sachdev, A. Gupta, and B. S. Sathyaprakash, *Phys. Rev. D* **105**, 104016 (2022), arXiv:2102.07692 [gr-qc].
- [37] J. Janquart, T. Baka, A. Samajdar, T. Dietrich, and C. Van Den Broeck, *Mon. Not. R. Astron. Soc.* **523**, 1699 (2023).
- [38] D. Gerosa and M. Bellotti, *Class. Quantum Grav.* **41**, 125002 (2024), arXiv:2404.16930 [astro-ph.HE].
- [39] J. Bradbury, R. Frostig, P. Hawkins, M. J. Johnson, C. Leary, D. Maclaurin, G. Necula, A. Paszke, J. VanderPlas, S. Wanderman-Milne, and Q. Zhang, github.com/google/jax (2018).
- [40] G. Pratten, S. Husa, C. García-Quirós, M. Colleoni, A. Ramos-Buades, H. Estellés, and R. Jaume, *Phys. Rev. D* **102**, 064001 (2020), arXiv:2001.11412 [gr-qc].
- [41] C. García-Quirós, M. Colleoni, S. Husa, H. Estellés, G. Pratten, A. Ramos-Buades, M. Mateu-Lucena, and R. Jaume, *Phys. Rev. D* **102**, 064002 (2020), arXiv:2001.10914 [gr-qc].
- [42] G. Pratten, C. García-Quirós, M. Colleoni, A. Ramos-Buades, H. Estellés, M. Mateu-Lucena, R. Jaume, M. Haney, D. Keitel, J. E. Thompson, and S. Husa, *Phys. Rev. D* **103**, 104056 (2021), arXiv:2004.06503 [gr-qc].
- [43] N. Aghanim et al., *Astron. Astrophys.* **641**, A6 (2020), arXiv:1807.06209 [astro-ph.CO].
- [44] V. Srivastava, D. Davis, K. Kuns, P. Landry, S. Ballmer, M. Evans, E. D. Hall, J. Read, and B. S. Sathyaprakash,

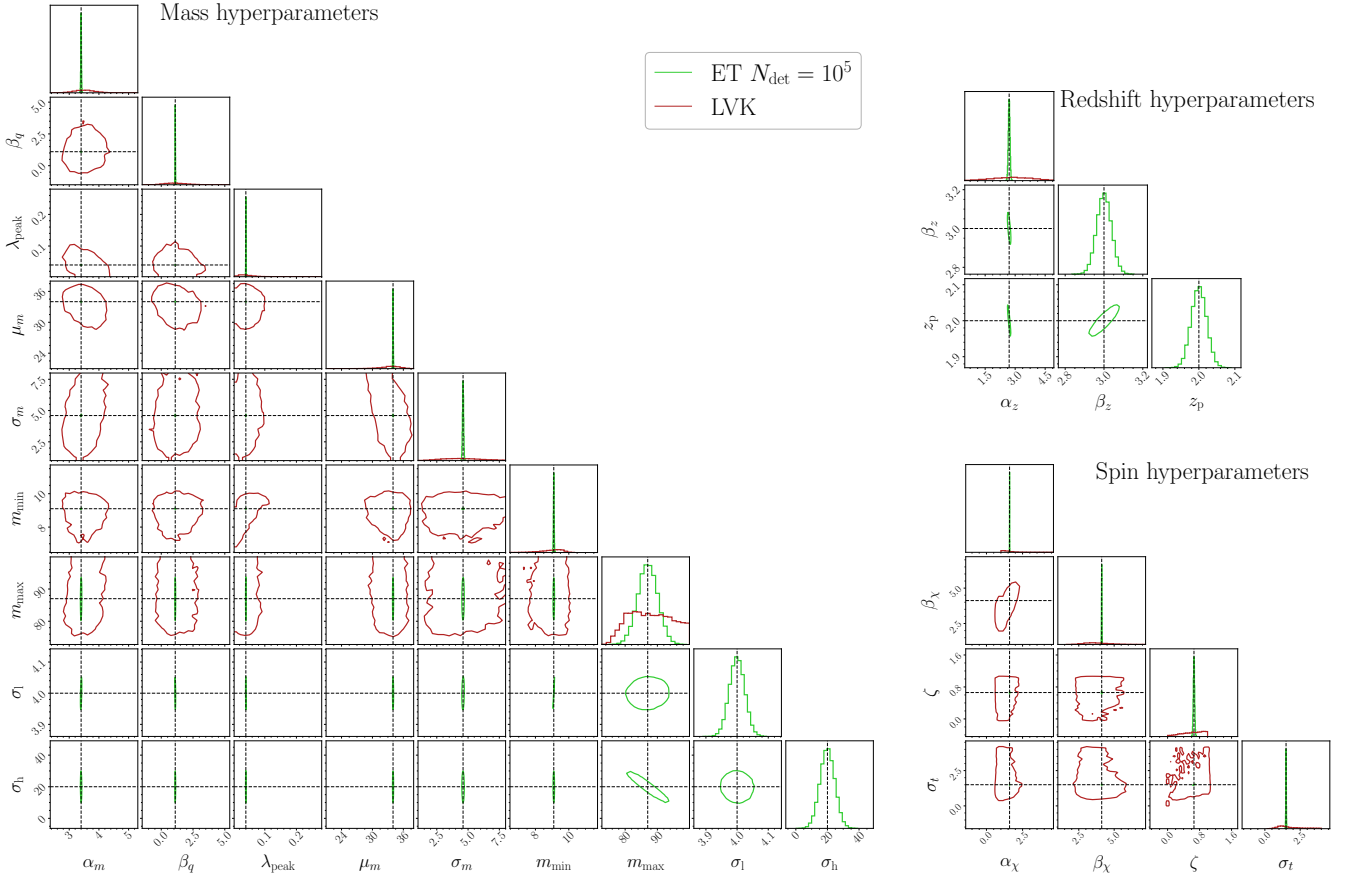


Figure 6. Same as Fig. 2 but comparing results assuming $N_{\text{det}} = 10^5$ detections with ET ($T_{\text{obs}} \sim 2$ yr, light curves) against current constraints from LIGO/Virgo data (LVK, dark curves). See App. B for important caveats.

- Astrophys. J.* **931**, 22 (2022), arXiv:2201.10668 [gr-qc].
- [45] M. Fishbach, D. E. Holz, and W. M. Farr, *Astrophys. J. Lett.* **863**, L41 (2018), arXiv:1805.10270 [astro-ph.HE].
- [46] C. Talbot and E. Thrane, *Astrophys. J.* **856**, 173 (2018), arXiv:1801.02699 [astro-ph.HE].
- [47] P. Madau and M. Dickinson, *Annu. Rev. Astron. Astrophys.* **52**, 415 (2014), arXiv:1403.0007 [astro-ph.CO].
- [48] C. Talbot and E. Thrane, *Phys. Rev. D* **96**, 023012 (2017), arXiv:1704.08370 [astro-ph.HE].
- [49] E. Payne, S. Banagiri, P. D. Lasky, and E. Thrane, *Phys. Rev. D* **102**, 102004 (2020), arXiv:2006.11957 [astro-ph.CO].
- [50] T. Kinugawa, K. Inayoshi, K. Hotokezaka, D. Nakauchi, and T. Nakamura, *Mon. Not. R. Astron. Soc.* **442**, 2963 (2014), arXiv:1402.6672 [astro-ph.HE].
- [51] M. Sasaki, T. Suyama, T. Tanaka, and S. Yokoyama, *Class. Quantum Grav.* **35**, 063001 (2018), arXiv:1801.05235 [astro-ph.CO].
- [52] K. K. Y. Ng, S. Chen, B. Goncharov, U. Dupletsa, S. Borhanian, M. Branchesi, J. Harms, M. Maggiore, B. S. Sathyaprakash, and S. Vitale, *Astrophys. J. Lett.* **931**, L12 (2022), arXiv:2108.07276 [astro-ph.CO].
- [53] M. Mancarella, F. Iacovelli, and D. Gerosa, *Phys. Rev. D* **107**, L101302 (2023), arXiv:2303.16323 [gr-qc].
- [54] K. Belczynski, A. Heger, W. Gladysz, A. J. Ruiter, S. Woosley, G. Wiktorowicz, H. Y. Chen, T. Bulik, R. O’Shaughnessy, D. E. Holz, C. L. Fryer, and E. Berti, *Astron. Astrophys.* **594**, A97 (2016), arXiv:1607.03116 [astro-ph.HE].
- [55] P. Marchant, M. Renzo, R. Farmer, K. M. W. Pappas, R. E. Taam, S. E. de Mink, and V. Kalogera, *Astrophys. J.* **882**, 36 (2019), arXiv:1810.13412 [astro-ph.HE].
- [56] S. Stevenson, M. Sampson, J. Powell, A. Vigna-Gómez, C. J. Neijssel, D. Szécsi, and I. Mandel, *Astrophys. J.* **882**, 121 (2019), arXiv:1904.02821 [astro-ph.HE].
- [57] S. E. Woosley, *Astrophys. J.* **836**, 244 (2017), arXiv:1608.08939 [astro-ph.HE].
- [58] N. Giacobbo and M. Mapelli, *Mon. Not. R. Astron. Soc.* **480**, 2011 (2018), arXiv:1806.00001 [astro-ph.HE].
- [59] K. Belczynski, J. Klencki, C. E. Fields, A. Olejak, E. Berti, G. Meynet, C. L. Fryer, D. E. Holz, R. O’Shaughnessy, D. A. Brown, T. Bulik, S. C. Leung, K. Nomoto, P. Madau, R. Hirschi, E. Kaiser, S. Jones, S. Mondal, M. Chruslinska, P. Drozda, D. Gerosa, Z. Doctor, M. Giersz, S. Ekstrom, C. Georgy, A. Askar, V. Baibhav, D. Wysocki, T. Natan, W. M. Farr, G. Wiktorowicz, M. Coleman Miller, B. Farr, and J. P. Lasota, *Astron. Astrophys.* **636**, A104 (2020), arXiv:1706.07053 [astro-ph.HE].
- [60] L. A. C. van Son, S. E. de Mink, M. Renzo, S. Justham, E. Zapartas, K. Breivik, T. Callister, W. M. Farr, and C. Conroy, *Astrophys. J.* **940**, 184 (2022), arXiv:2209.13609 [astro-ph.HE].
- [61] F. Antonini and F. A. Rasio, *Astrophys. J.* **831**, 187 (2016), arXiv:1606.04889 [astro-ph.HE].

- [62] H. Tagawa, Z. Haiman, and B. Kocsis, *Astrophys. J.* **898**, 25 (2020), arXiv:1912.08218 [astro-ph.GA].
- [63] D. D. Hendriks, L. A. C. van Son, M. Renzo, R. G. Izzard, and R. Farmer, *Mon. Not. R. Astron. Soc.* **526**, 4130 (2023), arXiv:2309.09339 [astro-ph.HE].
- [64] M. M. Briel, H. F. Stevance, and J. J. Eldridge, *Mon. Not. R. Astron. Soc.* **520**, 5724 (2023), arXiv:2206.13842 [astro-ph.HE].
- [65] G. Clark, A. Gonye, and S. J. Miller, (2021), arXiv:2101.08162 [stat.OT].
- [66] I. Mandel, C. P. L. Berry, F. Ohme, S. Fairhurst, and W. M. Farr, *Class. Quantum Grav.* **31**, 155005 (2014), arXiv:1404.2382 [gr-qc].
- [67] M. Fishbach and V. Kalogera, *Astrophys. J. Lett.* **914**, L30 (2021), arXiv:2105.06491 [astro-ph.HE].
- [68] L. A. C. van Son, S. E. de Mink, T. Callister, S. Justham, M. Renzo, T. Wagg, F. S. Broekgaarden, F. Kummer, R. Pakmor, and I. Mandel, *Astrophys. J.* **931**, 17 (2022), arXiv:2110.01634 [astro-ph.HE].
- [69] C. J. Neijssel, A. Vigna-Gómez, S. Stevenson, J. W. Barrett, S. M. Gaebel, F. S. Broekgaarden, S. E. de Mink, D. Szécsi, S. Vinciguerra, and I. Mandel, *Mon. Not. R. Astron. Soc.* **490**, 3740 (2019), arXiv:1906.08136 [astro-ph.SR].
- [70] F. Santoliquido, M. Mapelli, N. Giacobbo, Y. Bouffanais, and M. C. Artale, *Mon. Not. R. Astron. Soc.* **502**, 4877 (2021), arXiv:2009.03911 [astro-ph.HE].
- [71] I. Mandel and R. O’Shaughnessy, *Class. Quantum Grav.* **27**, 114007 (2010), arXiv:0912.1074 [astro-ph.HE].
- [72] C. L. Rodriguez, M. Zevin, C. Pankow, V. Kalogera, and F. A. Rasio, *Astrophys. J. Lett.* **832**, L2 (2016), arXiv:1609.05916 [astro-ph.HE].
- [73] D. Gerosa, E. Berti, R. O’Shaughnessy, K. Belczynski, M. Kesden, D. Wysocki, and W. Gladysz, *Phys. Rev. D* **98**, 084036 (2018), arXiv:1808.02491 [astro-ph.HE].
- [74] D. Gerosa and E. Berti, *Phys. Rev. D* **95**, 124046 (2017), arXiv:1703.06223 [gr-qc].
- [75] M. Fishbach, D. E. Holz, and B. Farr, *Astrophys. J. Lett.* **840**, L24 (2017), arXiv:1703.06869 [astro-ph.HE].
- [76] J. Fuller and L. Ma, *Astrophys. J. Lett.* **881**, L1 (2019), arXiv:1907.03714 [astro-ph.SR].
- [77] P. Madau and T. Fragos, *Astrophys. J.* **840**, 39 (2017), arXiv:1606.07887 [astro-ph.GA].
- [78] M. Dominik, E. Berti, R. O’Shaughnessy, I. Mandel, K. Belczynski, C. Fryer, D. E. Holz, T. Bulik, and F. Panarale, *Astrophys. J.* **806**, 263 (2015), arXiv:1405.7016 [astro-ph.HE].